Zeeshan Saeed[1]
Department of Mechanical Engineering,
Politecnico di Torino,
Corso Duca degli Abruzzi 24,
Turin 10129, Italy
e-mail: zeeshan.saeed@polito.it

Steven W. B. Klaassen[1]
Chair of Applied Mechanics,
Technical University of Munich,
Boltzmannstr. 15,
D-85748 Garching, Germany
e-mail: steven.klaassen@tum.de

Christian M. Firrone
Department of Mechanical Engineering,
Politecnico di Torino,
Corso Duca degli Abruzzi 24,
Turin 10129, Italy
e-mail: christian.firrone@polito.it

Teresa M. Berruti
Department of Mechanical Engineering,
Politecnico di Torino,
Corso Duca degli Abruzzi 24,
Turin 10129, Italy
e-mail: teresa.berruti@polito.it

Daniel J. Rixen
Chair of Applied Mechanics,
Technical University of Munich,
Boltzmannstr. 15,
D-85748 Garching, Germany
e-mail: rixen@tum.de

Experimental Joint Identification Using System Equivalent Model Mixing in a Bladed Disk

A joint between two components can be seen as a means to transmit dynamic information from one side to the other. To identify the joint, a reverse process called decoupling can be applied. This is not as straightforward as the coupling, especially when the substructures have three-dimensional characteristics, or sensor mounting effects are significant, or the interface degrees-of-freedom (DoF) are inaccessible for response measurement and excitation. Acquiring frequency response functions (FRFs) at the interface DoF, therefore, becomes challenging. Consequently, one has to consider hybrid or expansion methods that can expand the observed dynamics on accessible DoF to inaccessible DoF. In this work, we attempt to identify the joint dynamics using the system equivalent model mixing (SEMM) decoupling method with a virtual point description of the interface. Measurements are made only at the internal DoF of the uncoupled substructures and also of the coupled structure assuming that the joint dynamics are observable in the assembled state. Expanding them to the interface DoF and performing coupling and decoupling operations iteratively, the joint is identified. The substructures under consideration are a disk and blade —an academic test geometry that has a total of 18 blades but only one blade-to-disk joint is considered in this investigation. The joint is a typical dove-tail assembly. The method is shown to identify the joint without any direct interface DoF measurement.
[DOI: 10.1115/1.4047361]

Keywords: bladed-disks, joint identification, SEMM, virtual point, dynamic expansion, decoupling, dynamics, system identification

1 Introduction

Substructure identification in dynamic substructuring (DS) framework [1] has gained much attention in the last two decades. That is, an unknown subsystem is generally identified by decoupling a known subsystem from a known assembled system [2,3]. If the assembled system and all its subsystems are known, one can apply decoupling to identify the joint in between by introducing an appropriate joint model [4].

The classic decoupling methods [4,5] require that the dynamics at the interface are measured (or available) explicitly both at translational and rotational degrees-of-freedom (DoF) on a substructure. However, due to narrow spaces, the interface may be largely inaccessible for sensor mounting or excitation in all directions. Such an inability renders these methods applicable only to simpler substructures. For complex geometries, expansion methods are needed in order to extrapolate the dynamics measured on easy-to-measure DoF to those that are difficult-to-measure.

A modal expansion method called system equivalent reduction expansion process (SEREP) [6] expands the measured modes of substructures on their numerical modes. The so-called expanded modal basis can then be used to couple or decouple the substructures [7–9]. However, the modal expansion is restricted because one can only use in the expansion basis as many modes as the number of measured DoF, thereby limiting the measurement of higher modes. As a result, the system cannot be accurately represented at higher frequencies especially when the modal density is high, for example, in case of bladed-disks [10]. On the other hand, frequency-based substructuring (FBS) methods provide a great advantage due to the fact that the directly measured FRFs are utilized without any modal parameters estimation. A recently developed expansion method, system equivalent model mixing (SEMM) [11], based on the FBS formulation provides a direct and convenient way to expand the measured FRFs over the numerical FRFs. It is a method of coupling (and decoupling) different equivalent models of the same (sub)structure, namely, parent, overlay, and removed models. The output model is an expansion of the overlay model (measured dynamics) over the DoF of the parent model (numerical). Specifically, SEMM offers some benefits listed below:

(1) The measured FRFs in the overlay model do not need to be inverted. Inversion of measured matrices, as usually performed in substructure assembly, is known to cause spurious peaks in the experimental DS [12].
(2) FRFs can be expanded to the inaccessible boundary DoF by measuring accessible internal DoF, provided that the boundary DoF are observable.
(3) By virtue of the expansion, one can easily construct a collocated DoF set. By collocated, we mean that each DoF is an input as well as an output DoF resulting in square FRF matrices. Drive-point FRFs are in practice quite difficult to measure [13,14] and need special arrangements for good accuracy [9]. Note that the square matrices are an essential prerequisite for coupling (and decoupling) methods [4,5,15].

Other than SEMM, the FRFs can also be expanded at the inaccessible DoF in order to construct collocated FRFs, see for example,

[1]Corresponding authors.

Contributed by the Design Engineering Division of ASME for publication in the Journal of Vibration and Acoustics. Manuscript received February 14, 2020; final manuscript received May 18, 2020; published online June 19, 2020. Assoc. Editor: Matthew R.W. Brake.

Refs. [16,17]. Particularly, the round-trip theory [17] constructs the collocated FRFs by avoiding the excitations at the interface (or passive) DoF. However, the responses still have to be measured at the interface which may not be possible in many types of interfaces such as those found in bladed-disks [18,19]. Due to this limitation and the above-listed advantages of SEMM, it will be chosen in this work to expand the FRFs to the interface DoF.

In order to accurately capture the interface behavior, rotational information is also very important in experimental DS [12,20]. One possibility is to measure the rotations directly [21–23] by rotational accelerometers. However, these sensors are usually heavy and may only be suitable for bulky structures. Sensor loading becomes too significant for small-sized structural components. Therefore, one has to rely on calculating rotations either by finite difference [24] or by equivalent multi-point connection (EMPC) [25] with an interface consisting of a non-collinear DoF set. Based on the latter, the virtual point transformation method [26] transforms the measured translations to one or more virtual points, which describes the interface with both translations and rotations.

After one has acquired a collocated set of DoF consisting of translational and rotational interface DoF, the joint identification can be performed by the inverse substructuring or substructure decoupling methods. Inverse substructuring methods [15] assume that the joint elements (usually rubber isolators) have negligible mass. This allows for a way to decouple the *joint dynamic stiffness* from that of the total system without knowing the dynamics of the connected substructures, i.e., only the connection dynamics of substructures are to be known. In Refs. [27–29], this approach has been applied successfully to the resilient or flexible rubber joints. These methods are also often referred to as in-situ identification.

The substructure decoupling [2,4,5,30,31] can be applied to any (linear) joint model. In these methods, the joint dynamics are identified by decoupling the *substructure dynamic models* from the total system. As opposed to inverse substructuring, they require knowledge of the substructure internal and connection dynamics. Due to many difficulties encountered in experimental DS, these methods have been applied to only simpler cases. Even then, the identified joint parameters are strongly influenced by measurement errors and are usually frequency dependent [4,5,31]. A recent article [32] compares both the inverse substructuring and substructure decoupling methods applied on a rubber isolator.

The SEMM method can also be extended to substructure decoupling in order to identify the joint dynamics. It was applied on a numerical truss structure in Ref. [33]. The underlying assumption is that, in the assembled structure, the joint dynamics are implicitly and sufficiently observed by measurements at the internal DoF. Thus, the assembled (built-up) structure's measured FRFs can be overlaid on the uncoupled substructure models—obtained separately. The joint is then identified through decoupling of the assembled and the uncoupled models. The process can be iteratively applied until the joint properties have converged.

In this paper, the joint identification by the SEMM decoupling method [33] is applied to a case of an academic disk coupled to one blade. The particular shape of the joint between the disk and the blade (a dove-tail attachment) [18] makes the FRF measurements impossible at the interfaces. For this type of interface, it is essential that both the translational and rotational behavior is properly accounted for. The FRFs obtained through the impact testing campaign on the internal DoF of the blade and disk and also of their assembly are expanded and transformed to a virtual point description of the interface.

The paper is organized as follows: Section 2 recalls the theoretical background of the SEMM method starting from the theory of the FBS with rigid and flexible coupling between substructures. In Sec. 3, the experimental and numerical setup of a disk connected to one blade, used as a test geometry for the method, is described. In Sec. 4, after the validation of the SEMM method on each substructure, the results of validation on the assembled structure and the identified joint are presented followed by discussion and conclusions in Secs. 5 and 6, respectively.

2 Theory

In this section, the theoretical background of the SEMM decoupling method is presented. In the first part, dual formulation of Lagrange multiplier frequency-based substructuring (LM-FBS) is discussed followed by flexible coupling and decoupling. Then, it is explained how different equivalent models are obtained for all connecting substructures and how the dynamics are expanded to get the substructure hybrid models. Finally, the principles, on which the SEMM decoupling method is based, are explained in detail.

2.1 Frequency-Based Substructuring. The equation of motion of an sth substructure in frequency domain with displacement vector $\mathbf{u}^{(s)}$, external forces $\mathbf{f}^{(s)}$, and interface forces $\mathbf{g}^{(s)}$ is written as

$$\mathbf{Z}^{(s)}\mathbf{u}^{(s)} = \mathbf{f}^{(s)} + \mathbf{g}^{(s)} \tag{1}$$

where $s = 1, 2, \ldots, N$ is a substructure index and $\mathbf{Z}^{(s)}$ is the frequency ω-dependent dynamic stiffness:

$$\mathbf{Z}^{(s)} \triangleq \mathbf{Z}^{(s)}(\omega) \triangleq -\omega^2\mathbf{M}^{(s)} + i\omega\mathbf{C}^{(s)} + \mathbf{K}^{(s)} \tag{2}$$

where $\mathbf{M}^{(s)}$, $\mathbf{C}^{(s)}$, and $\mathbf{K}^{(s)}$ are time-invariant mass, damping, and stiffness matrices, respectively. The displacement vector $\mathbf{u}^{(s)}$ is composed of internal DoF $\mathbf{u}_i^{(s)}$ and boundary DoF $\mathbf{u}_b^{(s)}$ of substructure s, as shown in Fig. 1 for A and B, as an example. The substructure dynamic stiffness matrices, displacement, and force vectors are concatenated as block matrices and vectors, respectively, to express the uncoupled system of substructures.

$$\mathbf{Z} \triangleq \begin{bmatrix} \mathbf{Z}^{(1)} & & & \\ & \mathbf{Z}^{(2)} & & \\ & & \ddots & \\ & & & \mathbf{Z}^{(N)} \end{bmatrix}, \quad \mathbf{u} \triangleq \begin{Bmatrix} \mathbf{u}^{(1)} \\ \mathbf{u}^{(2)} \\ \vdots \\ \mathbf{u}^{(N)} \end{Bmatrix},$$
$$\mathbf{f} \triangleq \begin{Bmatrix} \mathbf{f}^{(1)} \\ \mathbf{f}^{(2)} \\ \vdots \\ \mathbf{f}^{(N)} \end{Bmatrix}, \quad \mathbf{g} \triangleq \begin{Bmatrix} \mathbf{g}^{(1)} \\ \mathbf{g}^{(2)} \\ \vdots \\ \mathbf{g}^{(N)} \end{Bmatrix} \tag{3}$$

In a measurement campaign, it is the FRF matrix that is measured and can be obtained in the forms of admittance, mobility, or acceleration. Denote the admittance matrix as $\mathbf{Y} \triangleq \mathbf{Z}^{-1}$. Equation of motion is then written for the uncoupled block matrices

$$\mathbf{u} = \mathbf{Y}(\mathbf{f} + \mathbf{g}) \tag{4}$$

The coupling of the substructures requires that the interface or boundary DoF are compatible in displacement which is ensured by a signed Boolean matrix $\mathbf{B}$ such that $\mathbf{Bu} = \mathbf{0}$ or $\mathbf{u}_b^{(s)} - \mathbf{u}_b^{(r)} = \mathbf{0}$ for $r = 1, 2, \ldots, N$. To satisfy the equilibrium at the boundary DoF, $\boldsymbol{\lambda}$ (known as Lagrange multipliers) are introduced such that $\mathbf{B}^T\lambda = -\mathbf{g}$. Substituting $\mathbf{g}$ in Eq. (4) and supplementing it with the compatibility equation gives the following system:

$$\begin{aligned} \mathbf{u} &= \mathbf{Y}(\mathbf{f} - \mathbf{B}^T\lambda) \\ \mathbf{Bu} &= \mathbf{0} \end{aligned} \tag{5}$$

Eliminating λ from this dual expression of the assembly yields the LM-FBS form:

$$\mathbf{u} = \mathbf{Yf} - \mathbf{YB}^T(\mathbf{BYB}^T)^{-1}\mathbf{BYf} \quad \Rightarrow \quad \mathbf{u} = \bar{\mathbf{Y}}\mathbf{f} \tag{6}$$

where $\bar{\mathbf{Y}}$ is the coupled admittance

$$\bar{\mathbf{Y}} = \mathbf{Y} - \mathbf{YB}^T(\mathbf{BYB}^T)^{-1}\mathbf{BY} \tag{7}$$

This is a dual formulation [34] consisting of DoF of all the substructures to be coupled. It requires that the driving point

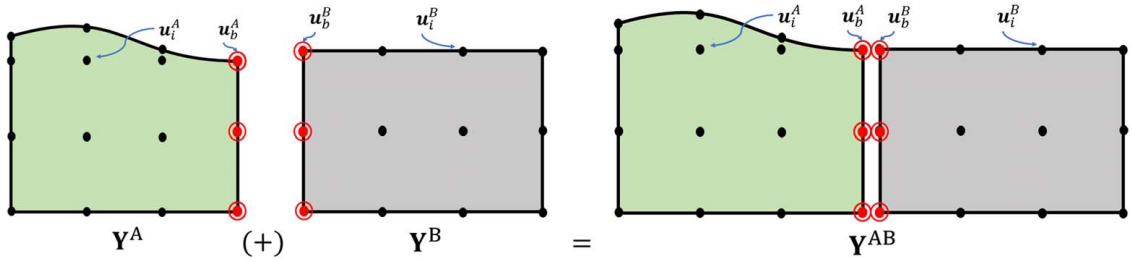

Fig. 1 A rigid coupling of two substructures A and B. The coupling exists only at the interface DoF by virtue of the compatibility condition, i.e., $u_b^A - u_b^B = 0$. Note that the DoF of both the substructures are shown in Y^{AB} signifying dual nature of the formulation.

admittances at the interface DoF can be measured (i.e., collocated displacement and force can be measured on the interface).

2.2 Flexible Coupling. The coupled substructure admittance given by Eq. (7) is a rigid coupling of the boundary DoF. Figure 1 graphically demonstrates this coupling with $\bar{\mathbf{Y}} = \mathbf{Y}^{\mathrm{AB}}$. Any two mating boundary DoF do not necessarily behave rigidly, and therefore, one needs to account for flexibility of the joint by introducing a joint model $\mathbf{Y}^{\mathrm{J}}$ between the two substructures. Including $\mathbf{Y}^{\mathrm{J}}$ in the uncoupled block diagonal admittance matrix $\mathbf{Y}$, the dually coupled LM-FBS admittance is calculated as:

$$\mathbf{Y}^{\mathrm{AJB}} = \mathbf{Y} - \mathbf{Y}\mathbf{B}^T(\mathbf{B}\mathbf{Y}\mathbf{B}^T)^{-1}\mathbf{B}\mathbf{Y}, \quad \text{with} \quad \mathbf{Y} = \begin{bmatrix} \mathbf{Y}^{\mathrm{A}} & & \\ & \mathbf{Y}^{\mathrm{J}} & \\ & & \mathbf{Y}^{\mathrm{B}} \end{bmatrix} \tag{8}$$

The matrix $\mathbf{B}$ in Eq. (8) applies compatibility between the substructures DoF and the joint DoF, as shown in Fig. 2. Theoretically, if mass is not considered in the joint, the dynamic stiffness of the joint is singular, and hence, the joint admittance $\mathbf{Y}^{\mathrm{J}}$ cannot be computed. This is discussed for a dummy joint identification in Sec. 4.2. The inclusion of the superscript $(\bullet)^{\mathrm{J}}$ in $\mathbf{Y}^{\mathrm{AJB}}$ is to emphasize that the joint dynamics are *explicitly* present in the coupled structure.

2.3 Joint Identification by Decoupling. Structures can be decoupled in a similar way as they are coupled by using fictitious admittance [2,3]. In detail, if admittances of the coupled (assembled) structure $\mathbf{Y}^{\mathrm{AJB}}$ and the associated substructures $\mathbf{Y}^{\mathrm{A}}$ and $\mathbf{Y}^{\mathrm{B}}$ are known, one can identify the joint $\mathbf{Y}^{\mathrm{J}}$ (c.f. Fig. 3) by adding A and B as negative substructures, namely,

$$\bar{\mathbf{Y}}^{J} = \mathbf{Y} - \mathbf{Y}\mathbf{B}^T(\mathbf{B}\mathbf{Y}\mathbf{B}^T)^{-1}\mathbf{B}\mathbf{Y}, \quad \text{with} \quad \mathbf{Y} = \begin{bmatrix} \mathbf{Y}^{\mathrm{AJB}} & & \\ & -\mathbf{Y}^{\mathrm{A}} & \\ & & -\mathbf{Y}^{\mathrm{B}} \end{bmatrix} \tag{9}$$

Note that here $\bar{\mathbf{Y}}^{\mathrm{J}}$ has the size of all the DoF of the coupled and the uncoupled structures and one needs to retain only the independent entries to obtain $\mathbf{Y}^{\mathrm{J}}$ [3].

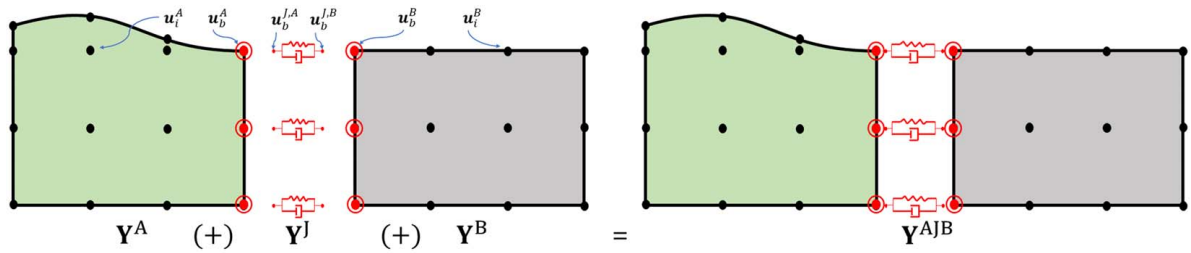

Fig. 2 Flexible coupling between substructures A and B by introducing a joint model consisting of a spring and a damper between the interface DoF of the substructures. The compatibility conditions read as $u_b^A - u_b^{J,A} = 0$ and $u_b^B - u_b^{J,B} = 0$.

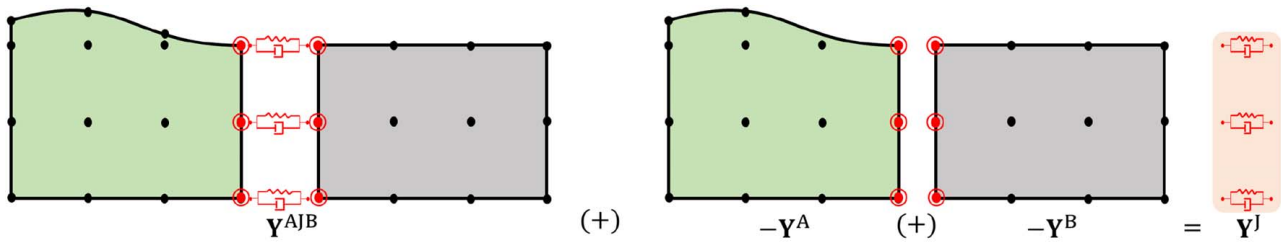

Fig. 3 Identification of the joint Y^J is done by coupling the assembled structure's admittance Y^{AJB} and fictitious admittances of the substructures Y^A and Y^B. The compatibility condition reads the same as in the case of coupling the joint in Fig. 2 (standard interface).

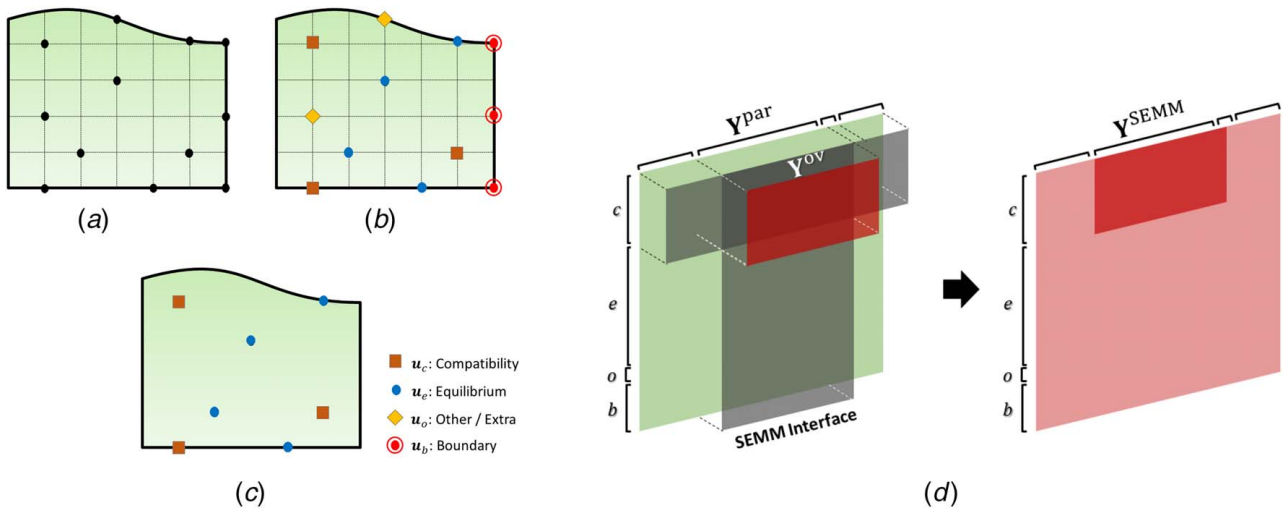

Fig. 4 (*a*) The reduced HCB model containing only master DoF set u_m. This is used as a parent model of the substructure. (*b*) The master DoF set is labeled according to the classification defined. (*c*) The overlay model that provides dynamics to the parent model. (*d*) Block matrix illustration of SEMM. Y^{par} is divided in four DoF sets vertically and horizontally.

In a coupling problem, the notion of the interface is standard, i.e., the compatibility and equilibrium are applied only at the interface DoF implying that the DoF are collocated. However, in a decoupling problem, the interface can be extended, i.e., the compatibility and equilibrium DoF need not be only at the boundary and can be extended to internal DoF resulting in an overdetermined interface [2,3,35]. In such a case, Eq. (7) can be generalized to the form:

$$\bar{\mathbf{Y}} = \mathbf{Y} - \mathbf{Y}\mathbf{B}_E^T \left(\mathbf{B}_C\ \mathbf{Y}\ \mathbf{B}_E^T\right)^+ \mathbf{B}_C\mathbf{Y} \tag{10}$$

where $\mathbf{B}_C$ and $\mathbf{B}_E$ are signed Boolean matrices for displacement DoF and equilibrium DoF, respectively, and $(\bullet)^+$ is the pseudo-inverse operator. In case of submodels coupling and decoupling of a substructure by SEMM (to be discussed next), its hybrid model is obtained by the extended interface notion.

2.4 Generating Substructure Hybrid Models by SEMM. The LM-FBS method requires explicitly the interface DoF in its classic formulation as presented in Eq. (6) including the drive-point FRFs. In many instances, these DoF are not accessible and substructure coupling or decoupling may not be performed directly. Therefore, expansion methods can be used to extrapolate the dynamic information to those DoF. One such method is SEMM [11] based on the LM-FBS whose inputs are a parent model $\mathbf{Y}^{\text{par}}$, an overlay model $\mathbf{Y}^{\text{ov}}$, and a removed model $\mathbf{Y}^{\text{rem}}$, and the output is a hybrid model $\mathbf{Y}^{\text{SEMM}}$ (or expanded numerical model). In this subsection, all the quantities belong to a substructure and not to a coupled structure. Therefore, the superscripts as component identifiers are omitted.

2.4.1 The Parent Model. The parent model in SEMM is a numerical model of the substructure under consideration that provides a DoF structure for the resulting hybrid model. It can be a full finite element (FE) or its reduced form, for example, a Hurty Craig-Bampton (HCB) model [36] to retain only the set of master DoF $\mathbf{u}_m$. In the latter case, the following relationship holds:

$$\begin{Bmatrix} \mathbf{u}_m \\ \mathbf{u}_s \end{Bmatrix} = \begin{bmatrix} \mathbf{I}_{mm} & \mathbf{0}_{ms} \\ \Psi_{sm} & \Phi_{ss} \end{bmatrix} \begin{Bmatrix} \mathbf{u}_m \\ \boldsymbol{\eta} \end{Bmatrix} = \mathbf{R} \begin{Bmatrix} \mathbf{u}_m \\ \boldsymbol{\eta} \end{Bmatrix} \tag{11}$$

where Ψ_{sm}, Φ_{ss} and η are constraint modes, a truncated set of fixed-interface modes and their modal amplitudes, respectively. The reduced mass and stiffness matrices are obtained by the transformation matrix $\mathbf{R}$ such that

$$\bar{\mathbf{M}} \triangleq \mathbf{R}^T\mathbf{M}\mathbf{R} \quad \text{and} \quad \bar{\mathbf{K}} \triangleq \mathbf{R}^T\mathbf{K}\mathbf{R} \tag{12}$$

The reduced model using the above reduced matrices is transformed to frequency domain by Eq. (2). Thus, the dynamic stiffness $\mathbf{Z}^{\text{par}}$ is expressed in the accelerance form[2] denoted here as $\mathbf{Y}^{\text{par}}$. This is the parent model in SEMM notation. Its DoF as illustrated in Fig. 4(*a*) can be grouped (Fig. 4(*b*)) as follows:

(1) Compatibility DoF $\mathbf{u}_c$ corresponds to the locations where response measurements are made.
(2) Equilibrium DoF $\mathbf{u}_e$ corresponds to the locations where impacts are applied
(3) Boundary DoF $\mathbf{u}_b$ belong to the interface of the substructure where it mates with another substructure. Their measurements may not be possible even in the unassembled state. Those DoF will be explicitly retained in the reduced model and their behavior will be obtained by the SEMM expansion.
(4) Other DoF $\mathbf{u}_o$ are extra DoF to be retained in the reduced model

With all the above DoF sets, denoted by the subscript g, the parent model $\mathbf{Y}^{\text{par}}$ in FRF matrix form is written as

$$\mathbf{Y}^{\text{par}} \triangleq \mathbf{Y}^{\text{par}}_{gg} \triangleq \begin{bmatrix} Y_{cc} & Y_{ce} & Y_{co} & Y_{cb} \\ Y_{ec} & Y_{ee} & Y_{eo} & Y_{eb} \\ Y_{oc} & Y_{oe} & Y_{oo} & Y_{ob} \\ Y_{bc} & Y_{be} & Y_{bo} & Y_{bb} \end{bmatrix}^{\text{par}} \quad \text{with} \quad \mathbf{u}_g^{\text{par}} \triangleq \begin{Bmatrix} \mathbf{u}_c \\ \mathbf{u}_e \\ \mathbf{u}_o \\ \mathbf{u}_b \end{Bmatrix}^{\text{par}} \tag{13}$$

2.4.2 The Overlay and Removed Models. The overlay model provides the dynamics of the substructure that are imposed on the parent model. In this case, these are all the measurement points, i.e., where the displacements (or accelerations) are measured as well as where the impact forces are applied. This model is shown in Fig. 4(*c*). A set of measured FRFs on the compatibility and equilibrium DoF on an actual structure gives the overlay model. Note that, in general, the DoF are not collocated, and hence, the overlay model is characterized by a rectangular FRF matrix with the following arrangement:

$$\mathbf{Y}^{\text{ov}} = \begin{bmatrix} Y_{ce} \end{bmatrix}^{\text{ov}} \tag{14}$$

The dynamics of the overlay model are superposed linearly on the parent model's dynamics, and therefore, the latter's own dynamics

[2]Accelerance is obtained by multiplying by $-\omega^2$ the inverse of the dynamic stiffness in the frequency domain.

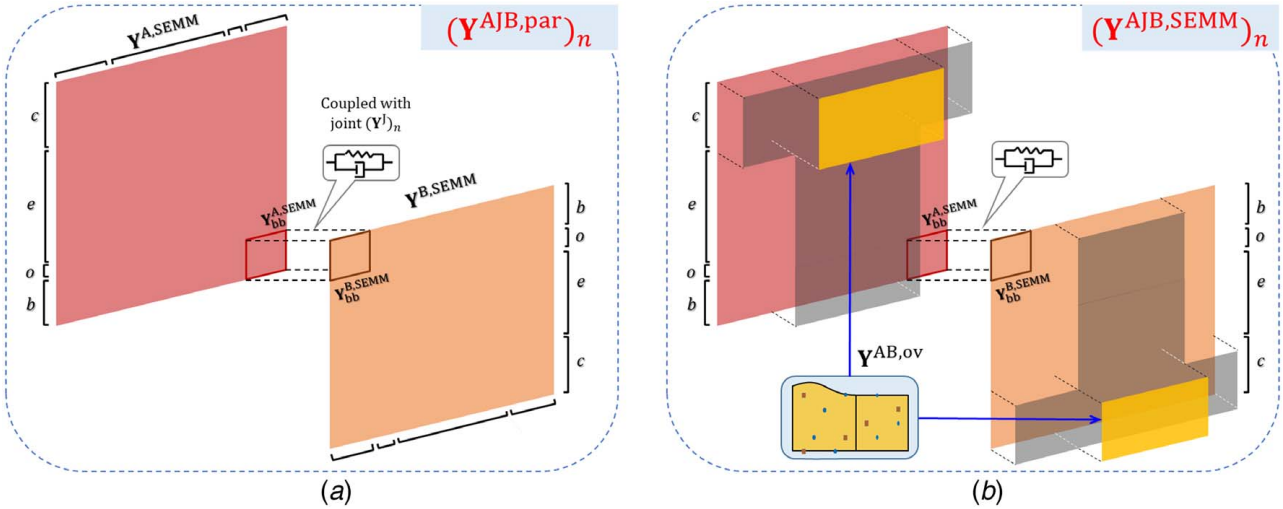

Fig. 5 A graphical representation of how the hybrid model for a coupled structure is obtained. (*a*) The parent model is made by coupling two hybrid models at the boundary DoF *b*. The DoF order for substructure B is reversed for this visual illustration. Adding a joint produces the coupled parent model $(\mathbf{Y}^{\mathrm{AJB,par}})_n$ at n^{th} iteration. (*b*) The coupled parent model together with the measurements of the assembled structure (overlay model) yields the coupled hybrid model $(\mathbf{Y}^{\mathrm{AJB,SEMM}})_n$. The overlay model DoF in the full-system measurements are also shown.

need to be decoupled by choosing a removed model. Thus, the removed model is set as the parent model, as proposed in Ref. [11].

$$\mathbf{Y}^{\mathrm{rem}} = \mathbf{Y}^{\mathrm{par}} \tag{15}$$

2.4.3 The Hybrid Model. The hybrid model $\bar{\mathbf{Y}}^{\mathrm{SEMM}}$ is obtained by coupling the overlay model with the parent model and decoupling at the same time the removed model. Using the appropriate Boolean matrices and the coupled accelerance in Eq. (10), the single-line expression is found in Ref. [11]

$$\bar{\mathbf{Y}}^{\mathrm{SEMM}} \triangleq \bar{\mathbf{Y}}^{\mathrm{SEMM}}_{gg} = \mathbf{Y}^{\mathrm{par}}_{gg} - \mathbf{Y}^{\mathrm{par}}_{gg}\,(\mathbf{Y}^{\mathrm{par}}_{cg})^{+}\,(\mathbf{Y}^{\mathrm{par}}_{ce} - \mathbf{Y}^{\mathrm{ov}}_{ce})\,(\mathbf{Y}^{\mathrm{par}}_{ge})^{+}\,\mathbf{Y}^{\mathrm{par}}_{gg} \tag{16}$$

It is to be clearly stated that the interface in SEMM is the extended interface related to the decoupled part of the information contained in $\mathbf{Y}^{\mathrm{rem}} = \mathbf{Y}^{\mathrm{par}}$. This can be understood by the fact that, the difference $(\mathbf{Y}^{\mathrm{par}}_{ce} - \mathbf{Y}^{\mathrm{ov}}_{ce})$ in Eq. (16) is propagated through the pseudo inverses $(\mathbf{Y}^{\mathrm{par}}_{cg})^{+}$ and $(\mathbf{Y}^{\mathrm{par}}_{ge})^{+}$ in the hybrid model. The so-called SEMM interface, depicted in Fig. 4(*d*) in gray color, shows two block matrices of $\mathbf{Y}^{\mathrm{par}}$, namely, *cg* and *ge*. Two important observations of the hybrid model $\bar{\mathbf{Y}}^{\mathrm{SEMM}}$ are that (i) it has the same DoF structure as $\mathbf{Y}^{\mathrm{par}}$ and (ii) it mimics the overlay model at all *ce* DoF (output to input), while on the other DoF, it acts as an expansion.

2.5 Virtual Point Interface Modes. The SEMM expansion allows for the access to the dynamics of the substructures at locations that can not be directly measured. These locations (DoF) can be selected on mating surfaces of the substructures. Note that any noise or measurement inconsistencies are also present in the expanded dynamics on these DoF. In order to reduce this effect on the dynamics delivery by SEMM on the boundary DoF, virtual points (VP) can be created as representative interface (see Fig. 7(*a*) for two VP interface on the blade test-case). This transformation is done by creating virtual point interface displacement $\mathbf{T}_u$ and force modes $\mathbf{T}_f^T$ at one or more virtual points [26].

$$\mathbf{Y}^{\mathrm{A,SEMM}} = \mathbf{T}_u^{\mathrm{A}}\;\bar{\mathbf{Y}}^{\mathrm{A,SEMM}}\;(\mathbf{T}_f^{\mathrm{A}})^T \tag{17}$$

The transformation, as mentioned in Sec. 1, leads to an interface that is described by both translations and rotations at the virtual point DoF. Similarly, the same transformation for substructure B can be done to get $\mathbf{Y}^{\mathrm{B,SEMM}}$.

2.6 Decoupling by SEMM. In Sec. 2.4, the hybrid models were created for each substructure whose parent models were the equivalent FE models. On the contrary, if joint dynamics are observable when the structure is in an assembled state, an FE model is not considered as an equivalent model because it lacks the joint dynamics. Therefore, an assembled system's parent model is created from the previous substructure hybrid models with a joint $\mathbf{Y}^{\mathrm{J}}$. The already created substructure hybrid models can be used to construct a version *n* of the parent model $(\mathbf{Y}^{\mathrm{AJB,par}})_n$ for the coupled structure; calculated from Eq. (8) rewritten here with a joint

$$(\mathbf{Y}^{\mathrm{AJB,par}})_n = \mathbf{Y}_n - \mathbf{Y}_n\mathbf{B}^T(\mathbf{B}\mathbf{Y}_n\mathbf{B}^T)^{-1}\mathbf{B}\mathbf{Y}_n, \quad \text{with}$$
$$\mathbf{Y}_n = \begin{bmatrix} \mathbf{Y}^{\mathrm{A,SEMM}} & & \\ & (\mathbf{Y}^{\mathrm{J}})_n & \\ & & \mathbf{Y}^{\mathrm{B,SEMM}} \end{bmatrix} \tag{18}$$

where $n = 0, 1, 2, \ldots$ denotes the iteration number to signify the iterative nature of the process as the joint $\mathbf{Y}^{\mathrm{J}}$ (to be identified) is not known a priori. This will be further explained shortly. The compatibility needs to be satisfied at the physical boundary DoF between the substructures, as presented in Sec. 2.2 and shown in Fig. 2. The assembled system's parent model is graphically illustrated in Fig. 5(*a*).

A set of measurements on the assembled structure provides the overlay model for the assembly. In order for the mass of the sensors not to affect the identification procedure, the locations of the sensors in assembly testing should be the same as they were in the component testing. In this way, the sensors are effectively considered a part of the system. The overlay model $\mathbf{Y}^{\mathrm{AB,ov}}$ contains the joint dynamics implicitly, and the FRFs are stored as

$$\mathbf{Y}^{\mathrm{AB,ov}} = \left[\, Y^{\mathrm{AB}}_{ce} \,\right]^{\mathrm{ov}} \tag{19}$$

Here, the subscripts *c* and *e* correspond to all the compatibility and equilibrium DoF on the "coupled structure" AB with the former being the output (response) DoF and the latter being the input (impact) DoF. The removed model is again the same as the coupled parent model in Eq. (18). The coupled structure's

hybrid model $(\mathbf{Y}^{\mathrm{AJB,SEMM}})_n$ is calculated from Eq. (16). These models are shown in a pictorial matrix form in Fig. 5(*b*).

To identify the joint dynamics between two substructures A and B, we assume that we have trustworthy hybrid models of the substructures $\mathbf{Y}^{\mathrm{A,SEMM}}$ and $\mathbf{Y}^{\mathrm{B,SEMM}}$, as explained earlier. To couple these submodels, we make a first estimate of the interface dynamics $(\mathbf{Y}^{\mathrm{J}})_0$ to build a first estimate of the assembly $(\mathbf{Y}^{\mathrm{AJB,\,par}})_0$ which will be improved with measurements on the assembly $\mathbf{Y}^{\mathrm{AB,ov}}$ by the SEMM procedure $(\mathbf{Y}^{\mathrm{AJB,SEMM}})_0$. An improved estimate of the joint $(\mathbf{Y}^{\mathrm{J}})_1$ is then evaluated from this updated assembly model by decoupling substructures A and B. This is done by using the standard interface decoupling procedure explained earlier in Eq. (9) where now $\mathbf{Y}^{\mathrm{A}} = \mathbf{Y}^{\mathrm{A,\,SEMM}}$, $\mathbf{Y}^{\mathrm{B}} = \mathbf{Y}^{\mathrm{B,\,SEMM}}$, and $\mathbf{Y}^{\mathrm{AJB}} = (\mathbf{Y}^{\mathrm{AJB,\,SEMM}})_0$. The new joint estimate $(\mathbf{Y}^{\mathrm{J}})_1$ is then used to create a new assembly model $(\mathbf{Y}^{\mathrm{AJB,par}})_1$ that is again updated $(\mathbf{Y}^{\mathrm{AJB,SEMM}})_1$ with the same measurements $\mathbf{Y}^{\mathrm{AB,ov}}$ and from which a further estimate of the joint dynamics $(\mathbf{Y}^{\mathrm{J}})_2$ is obtained by decoupling A and B. This iterative procedure can be repeated, assuming it converges to a joint for which the discrepancy between the model of the assembly and the measurements are minimized. This strategy was first proposed in Ref. [33] and applied to a simple numerical truss structure. It is outlined in a different manner and applied to a complex interface in this paper. It is worth noting that the initial joint $(\mathbf{Y}^{\mathrm{J}})_0$ can be blank (no coupling) or defined by the user. This is because the assembled parent model will anyway be updated by the measurements on the assembly in which the joint dynamics are assumed to be observable.

It is interesting to point out that, when integrating the measured information in the parent model for the assembly, the inverses in Eq. (16) can be computed as weighted pseudo inverse. A diagonal weighting matrix $\mathbf{W}$ having different weights w for the DoF set is defined

$$\mathbf{W} = \mathrm{diag}(w_c, w_e, w_o, w_b) \tag{20}$$

where the subscripts of w correspond to the same set of DoF as before. Dropping the superscript of the coupled parent model's accelerance $\mathbf{Y}^{\mathrm{par}}$ for clarity, the right-side pseudo-inverse in Eq. (16) is then given by

$$\mathbf{Y}_{cg}^{+} = \mathbf{W}\ \mathbf{Y}_{cg}^{T}(\mathbf{Y}_{cg}\ \mathbf{W}\ \mathbf{Y}_{cg}^{T})^{-1} \tag{21}$$

and the left-side pseudo inverse

$$\mathbf{Y}_{ge}^{+} = (\mathbf{Y}_{ge}^{T}\mathbf{W}\mathbf{Y}_{ge})^{-1}\mathbf{Y}_{ge}^{T}\mathbf{W} \tag{22}$$

The above expressions hold if $\mathbf{Y}_{cg}$ has full row rank and $\mathbf{Y}_{ge}$ has full column rank. In case of rank deficiency or ill-conditioning, the inverses can be computed by singular value decomposition with the smallest singular values truncated.

The weighted pseudo-inverses help expand the dynamics to the unmeasured DoF in a weighted least squares sense. Particularly, the physical boundary DoF $\mathbf{u}_b$ are assigned a higher weighting factor because these are the DoF to be identified in the process. The solution converges fast with such weights as shown in the Appendix.

2.6.1 Summary of the Decoupling Method. The linear SEMM decoupling process can be briefly summarized as follows:

(1) Get hybrid models of each substructure $\mathbf{Y}^{\mathrm{A,SEMM}}$ and $\mathbf{Y}^{\mathrm{B,\,SEMM}}$ as outlined in Secs. 2.4 and 2.5.
(2) Perform measurements on the coupled structure on the same sensor and impact points as in the unassembled condition to get the coupled overlay model $\mathbf{Y}^{\mathrm{AB,ov}}$.
(3) Create the coupled parent model $(\mathbf{Y}^{\mathrm{AJB,par}})_n$ as per Eq. (18) with an estimated joint $(\mathbf{Y}^{\mathrm{J}})_n$.
(4) Obtain the hybrid model $(\mathbf{Y}^{\mathrm{AJB,SEMM}})_n$ from the estimated parent model $(\mathbf{Y}^{\mathrm{AJB,par}})_n$ and the overlay model $\mathbf{Y}^{\mathrm{AB,ov}}$ using Eq. (16).
(5) Perform decoupling as per Eq. (9) to obtain the joint $(\mathbf{Y}^{\mathrm{J}})_{n+1}$.
(6) Repeat Steps 3–5 until the expansion error $\|(\mathbf{Y}_{ce}^{\mathrm{AJB,par}})_n - \mathbf{Y}^{\mathrm{AB,ov}}\|$ is minimized.

3 Experimental and Numerical Setup

The test-case for application of the method is a disk with 18 slots in which as many blades can be connected, as shown in Fig. 6. In the present study, only one blade is connected to its respective slot since only one joint is considered.

The application of the SEMM decoupling method requires an experimental campaign with measurements of FRFs at internal DoF of both blade and disk in three measurement setups: (1) blade only, (2) disk only, and (3) coupled disk-blade. In detail, the three setups were arranged as follows:

(1) Blade suspended on flexible wires (Fig. 6(*a*)).
(2) Disk rigidly connected by six bolts to a cylindrical attachment (Fig. 6(*b*)).
(3) Disk coupled with the blade (Fig. 6(*c*)) where the disk is rigidly connected as above and the blade is pushed on the base of its root by a pin. The pin keeps the blade-root in contact with the surfaces of the disk slot (as can be seen in Fig. 6(*c*)).

Five tri-axial accelerometers are positioned on the blade and five on the disk. During the FRFs measurement campaign, an instrumented hammer is used for the excitation. For practical experimental reasons, the impact excitation points are never coincident with the measurement points where the accelerometers are positioned.

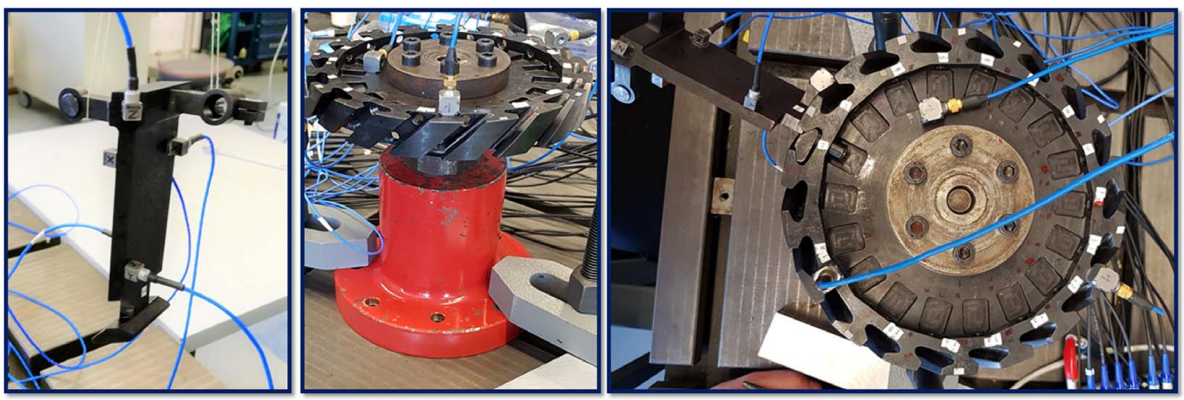

Fig. 6 The experimental setup with all the accelerometers mounted on (*a*) the blade hanged by wires, (*b*) the disk fixed at its center, and (c) the coupled blade and disk with the same constraint conditions as the disk

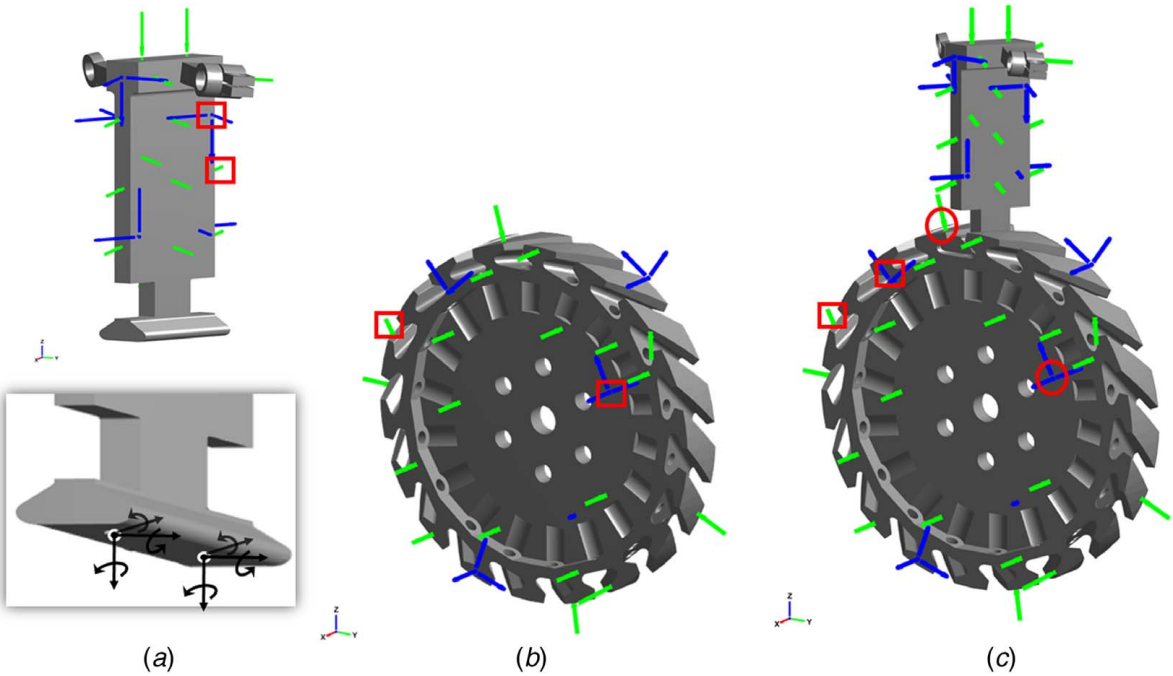

Fig. 7 The geometric models of the blade and disk showing the impacts' positions. The triads denote the response channels (triaxial accelerometers) and the single arrows denote the impact points. The markers (squares and circles) indicate the DoF used to validate the SEMM method to be discussed in Sec. 4. The interface consisting of two virtual points is depicted on the blade geometry.

Figure 7 shows the locations of both the impacts and the accelerometer channels as single arrows and triads, respectively. It must be noted that the measurement and impact points remain the same in the coupled configuration (Fig. 7(*c*)), in order to decouple the effect of sensor mass loading. As it can be observed from the figures, the impacts and accelerometers are made only at the internal DoF. This means that the FRFs are not measured on the interface (joint surface); neither on the blade root nor in the disk slot. The interface FRFs are, thus, derived through the SEMM technique, as explained in Section 2.

It is assumed that the coupled system behaves linearly since the energy of the impacts is not so high to introduce slip in the interface. Therefore, the SEMM approach for assembling and decoupling as proposed here is thus licit.

Recalling that the SEMM needs a parent (numerical) model of each substructure, FE models in ANSYS were created for both the blade and the disk. These FE models were then reduced by HCB transformation to retain only the physical master DoF together with 200 fixed-interface eigen modes, according to Eq. (11). The retained master DoF include all the internal DoF in Figs. 7(*a*) and 7(*b*) as well as the boundary DoF on the joint surfaces. The parent models according to the SEMM terminology are then obtained by computing the accelerance FRFs.

As described in Sec. 2.5, the interface between the blade and disk is modeled by using virtual points (VPs). For this test-case, two VPs are considered on each substructure [18] where each VP consists of three translations and three rotations. The two VPs are depicted on the blade-root in Fig. 7(*a*). Thus, the joint is represented by a 24 × 24 DoF system.

4 Results

This section presents application and validation of the method to identify the joint by the process explained in Sec. 2 and for the setup shown in Sec. 3. First, we present the results for the uncoupled blade and disk as validation of the SEMM method in Sec. 4.1. A numerical dummy joint is introduced between the two substructures in Sec. 4.2 to verify the SEMM decoupling method, presented in Sec. 2.6. The actual joint between the two components is then identified in Sec. 4.3 with a discussion on the joint in Sec. 4.4.

4.1 Validation of SEMM for Substructures. In the SEMM method, the overlay model is a set of experimental FRFs that provide the dynamics at some DoF to the parent model. For validation purpose, a group of this experimental FRFs was kept out of the overlay model as reference measurements, designated as $\mathbf{u}_o$ and shown with the red square markers in Figs. 7(*a*) and 7(*b*). On the same group, the SEMM expansion was performed. The resulting expanded FRFs are compared with those reference measurements. Figure 8 shows the validation of the SEMM method for both the single blade and single disk FRFs. In Fig. 8(*a*), the FRF predicted by SEMM is overlapping well with the experimental one for the blade. In particular, we see that the SEMM model corresponds much better than the parent numerical model to the measurement in the three resonance peaks in the frequency range, correcting the numerical model for sensor mass-loading and non-modeled damping. It is, however, to be observed that around 900 Hz, the location of the anti-resonance that was well predicted by the parent numerical model is actually getting worse in the SEMM model. This can be understood by the fact that anti-resonances depend on the location of the input and of the output and thus any error in location and orientation of the input or output sensors creates a shift in the anti-resonance frequencies. Small imperfections that can be hardly avoided when determining the location and orientation of our sensors are most probably the cause of this effect in our results.

The FRFs predicted by SEMM for the disk in Fig. 8(*b*) do not agree so well with the experiment. This discrepancy between numerical, experimental, and SEMM case is attributed to the reasons listed below:

(1) The numerical model of the disk does not take into account the masses of the accelerometers. They alter the cyclic symmetry of the disk—an effect not present in the numerical model.

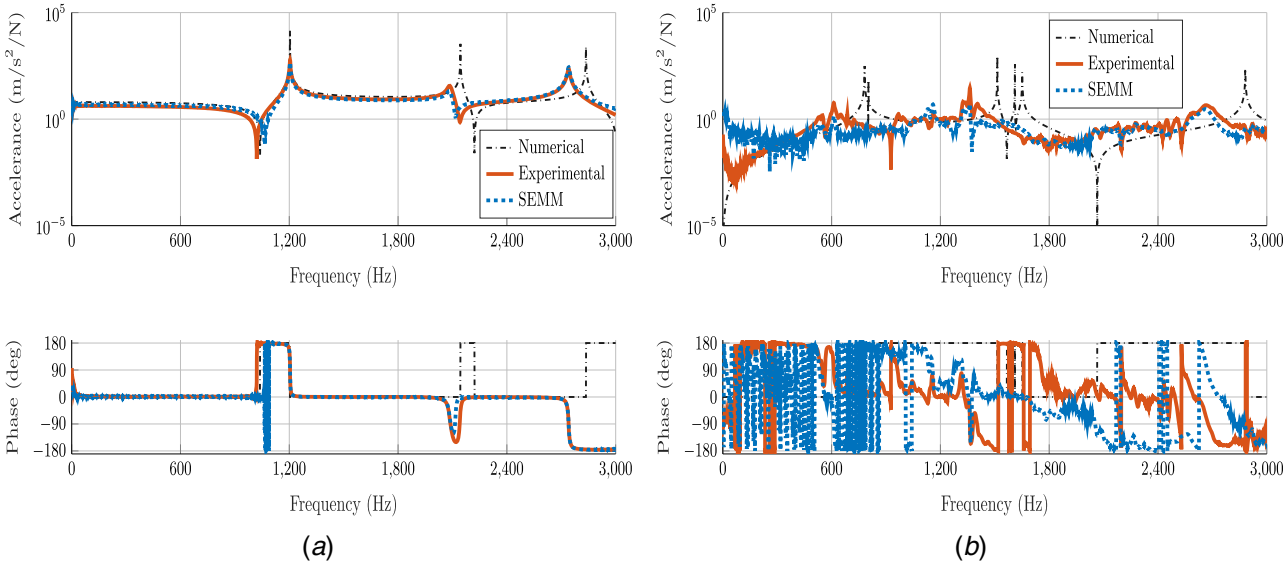

Fig. 8 FRFs for the SEMM validation of (*a*) blade and (*b*) disk at the DoF marked with squares in Figs. 7(*a*) and 7(*b*), respectively. The numerical FRFs were computed without any damping. The expanded FRF (legend: SEMM) for the blade agrees well with the experimental reference; whereas for the disk, it has lesser agreement in some regions.

(2) Most importantly, the constraints applied to the disk's FE model to fix its center do not correspond exactly to the actual constraint condition of the disk. Actually, the disk center is connected to a flanged-type fixture which is attached rigidly to a bench, see Fig. 6(*b*). The fixture introduces some of its own dynamics in the frequency band. While modeling the same fixture (along with the disk) in ANSYS, the displacement boundary condition is not ideally matched with the actual setup [37].

Generally, SEMM is affected when the mode shapes of the numerical model are no longer representative, which might be the case in this scenario [11]. In the future, the numerical models should be updated to include these effects, especially point two. However, considering the relatively small discrepancies between the experimental and hybrid model of the disk, the FRFs in Fig. 8(*b*) were deemed acceptable. For the following discussion, these hybrid (SEMM) models of both blade and disk were used to make the parent model of the coupled structure, as described in Sec. 2.6.

4.2 Verification of the Strategy by a Dummy Joint. The next step was to validate the iterative SEMM decoupling method. The idea was to introduce a joint between the blade and the disk whose parameters are known in advance (Table 1). The method is then applied to verify if it is able to identify these known parameters.

Between the two components' expanded models $\mathbf{Y}^{\mathrm{A,SEMM}}$ and $\mathbf{Y}^{\mathrm{B,SEMM}}$, the dummy-joint FRF model $\mathbf{Y}^{\mathrm{J,dum}}$ is introduced to create a *dummy-coupled* model that we then used to generate simulated measurements instead of the actual experimental measurements of the full-system. This ensures that measurement and expansion errors are the same for both the coupled and uncoupled models. If the internal DoF can observe the dynamics at the boundary—a minimum requirement for the SEMM expanded identification—then our proposed iterative strategy should be able to identify the interface dynamics. The reverse formulation is also true: if the joint is properly identified, then the internal DoF fully observe and control the boundary DoF and the decoupling step itself is validated. The dummy joint is a simple one-to-one mass-spring-damper system with the parameters[3] in Table 1.

Figure 9 shows the identified dummy dynamic stiffnesses along the frequency axis for translational and rotational DoF. In each figure, there are two joint identification plots for different weights of weighted pseudo-inverses discussed in Sec. 2.6. Focusing on the identified stiffness for the case of $w_b = 1 \times 10^8$ (with all the other DoF assigned a weight of 1), the figure shows that, with the exception of spurious effects, the dynamic stiffness of the dummy joint can be identified. The spurious effects are spread across the whole frequency band but pronounced in the region between 0 and 500 Hz in which the disk expanded model has some discrepancies. In this region, it is assumed that the boundary dynamics are not uniquely observed. The same is true for frequency regions near 1200 and 2100 Hz where sub-system resonances of the blade are observed in the FRF of Fig. 8(*a*). In these resonance regions, the identification can be influenced by the internal subsystems. Its reason and a way to mitigate it are discussed later.

In fact, by the method outlined in Sec. 2.6, the *dummy-coupled* system's dynamics are to be expanded on its coupled parent model, and subsequently, the joint is to be identified. The expansion occurs uniformly (if no weightings are assigned to $\mathbf{u}_b$) all over the DoF through the SEMM interface (Fig. 5(*b*)). This is where the subsystem's internal influence comes into play, including resonances[4] and noise in the hybrid models, i.e., through the pseudo-inverses in Eq. (16). If one of the subsystem is near resonance, the expansion would occur through the ill-conditioned matrices, and hence, the errors propagate also to the interface which are later identified and dubbed as the joint. Forcing the SEMM method to observe only the interface could easily rectify this problem, e.g., by

Table 1 Parameters of the dummy joint

	Translational	Rotational
Stiffness	1×10^7 N/m	1×10^4 Nm/rad
Damping	1×10^3 Ns/m	1×10^2 Nms/rad
Mass	5 g	5 gm^2/rad

[3]The mass in the joint parameters of Table 1 exists to easily create a non-singular system. In order to obtain the accelerance matrix, the dynamic stiffness is to be inverted which is singular without the mass (also see Sec. 2.2). Note that the mass is not necessarily present in the true joint.

[4]Note that the internal subsystem influence does not apply to a single substructure being expanded by SEMM because it is not composed of subsystems. This is also why the weightings were not discussed before Sec. 2.6 and in Sec. 4.1. However, there is no restriction on using them on a single substructure.

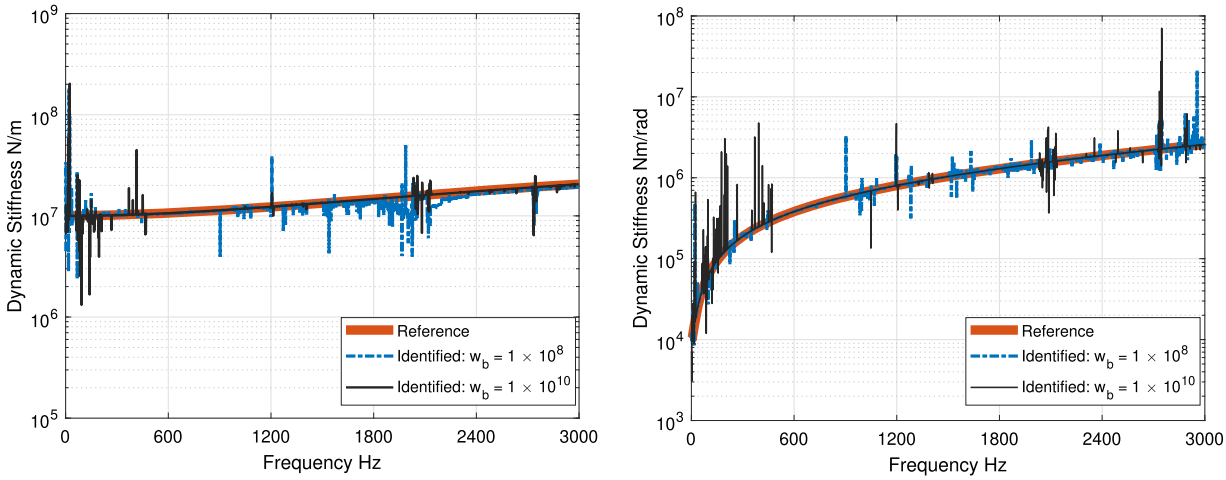

Fig. 9 The reference and identified dynamic stiffness of the dummy joint for: (*a*) Translational DoF and (*b*) rotational DoF on one of the two virtual points depicted on the blade in Fig. 6(*a*). The identified stiffness plots are obtained after three iterations. In the first iteration, no initial guess was used, i.e., the substructures were left uncoupled.

inclusion of a stronger weight toward interface DoF $\mathbf{u}_b$ or by ignoring internal DoF altogether through the weighted pseudo-inverses (see Appendix). By doing so, the internal subsystem's resonances or errors are not expanded to the interface or the joint.

The dummy joint of Fig. 9 with $w_b = 1 \times 10^8$ has identified some of the characteristics that belong to the internal subsystem, as discussed earlier. By further suppressing the weight of internal DoF would reduce the influence of those errors. This is evident by the identified joint with $w_b = 1 \times 10^{10}$ shown as the black stiffness line. The spurious errors throughout the frequency band have decreased and localized. Further increasing w_b would suppress more the internal subsystem influence but could also significantly deteriorate the numerical conditioning of the pseudo inverses in Eq. (16). The spurious errors are, nevertheless, easily recognizable as such and could be ignored in standard fitting or parametrization techniques.

4.3 Identification of the Actual Joint. After being validated on a known dummy joint, the method is applied to the identification of the actual joint in this section. We recall that the SEMM decoupling in Sec. 2.6 is an iterative and weighting the pseudo-inverses in Eq. (16) helps in faster convergence. The convergence of the joint identification strategy strongly depends on the weightings and is further described in the Appendix. In the following discussion on the actual joint identification, the presented results are, obviously, extracted from a converged system. The identification process was validated in two different steps.

In the first step, here called *self-validation*, all the measured FRFs are included in the overlay model of the assembled disk and blade $\mathbf{Y}^{\mathrm{AB,ov}}$. It is called *self-validation* because the set of expanded FRFs $\mathbf{Y}^{\mathrm{AJB,SEMM}}$ used in the identification process of the joint $\mathbf{Y}^{\mathrm{J}}$ (Sec. 2.6) are at the same DoF as in $\mathbf{Y}^{\mathrm{AB,ov}}$. The resulting agreement check between the measured and the recoupled FRFs ($\mathbf{Y}^{\mathrm{A,SEMM}}$, $\mathbf{Y}^{\mathrm{J}}$, and $\mathbf{Y}^{\mathrm{B,SEMM}}$) should be a trivial comparison which is shown in Fig. 10. Ideally, the FRF of the recoupled system labeled as "Coupled with Joint" should overlap the reference measurement at all frequencies which is however not the case. Note that the FRF labeled "Reference" was measured on the circle marked DoF in Fig. 7(*c*) and was included in the identification procedure. This shows that, in the joint identification process, the self-validation step is not so trivial. Indeed, it is assumed that the only difference between the coupled and uncoupled models was the existence of joint dynamics. Theoretically, this may be true but practically other differences exist between the coupled and uncoupled measurements, and the method cannot discriminate between them. This is the reason why the joints are generally noisy and sensitive to measurement and expansion bias errors [4,5,31].

In Fig. 10, the dotted curve named as rigid coupling is the FRF obtained by rigidly coupling the blade and the disk models ($\mathbf{Y}^{\mathrm{A,SEMM}}$and $\mathbf{Y}^{\mathrm{B,SEMM}}$), without any joint between them. From the comparison of the rigid coupling and the Reference FRFs, it can be noted that they are poorly overlapping. This confirms that the there is a significant contribution of the joint flexibility $\mathbf{Y}^{\mathrm{J}}$ to the dynamics of the assembled system, which cannot be modeled just with a rigid connection between the blade and disk.

In the second step of validation, here called *on-board validation*, we kept out from the measured FRFs of the assembled system (disk plus blade) some FRFs in order to use them only as reference for validation. This approach is the same as for SEMM validation on the single component blade or disk in Sec. 4.1. In the field of transfer path analysis (TPA)—a field narrowly related to joint identification—this type of validation is often referred to as an *on-board* or *in-situ* validation, and it can be performed in the same measurement campaign. This is more restrictive than the *self-validation* step since

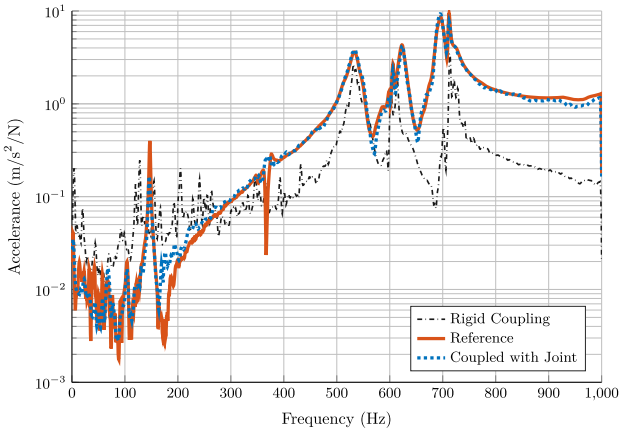

Fig. 10 The agreement of the FRF before and after identification. The solid validation line is a measured FRF of the full-system labeled "Reference" (measured on circle marked DoF in Fig. 7(c)). The dotted line indicates the coupled results (with the joint identified by the SEMM procedure). The dash-dotted line is the would-be rigid coupling (without joint). The coupled results are in agreement with the full-system reference FRF.

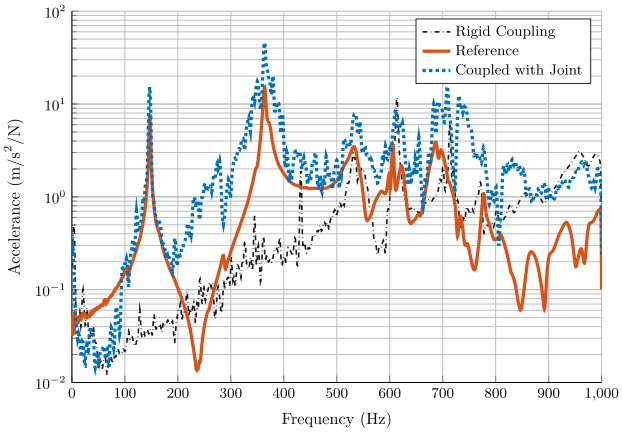

Fig. 11 The on-board validation of the joint. The solid validation line is a measured FRF of the full-system. This FRF (at the DoF marked with squares in Fig. 7(c)) has not been used to identify the joint. The dotted line indicates the coupled results (with the joint identified by the SEMM procedure). The dash-dotted line is the would-be rigid coupling (without joint). The coupled results are not in good agreement with the full-system reference FRF but outperform the rigid coupling.

the measured FRFs considered as reference are not included in the procedure of the joint identification, but they are kept only for validation purposes.

In Fig. 11, one of the measured FRFs, retained for validation is named as reference. On the same DoF (see Fig. 7), the FRF obtained after the identification procedure and recoupled $\mathbf{Y}^{A,SEMM}$, $\mathbf{Y}^{J}$, and $\mathbf{Y}^{B,SEMM}$, is labeled as coupled with Joint. The comparison of these two FRFs is acceptable but, as expected, not so good as in Fig. 10. The coupled with Joint FRF is more noisy than the Reference one and its amplitude is higher throughout the frequency band. However, the resonance frequencies are well captured and it can be noted that the FRF of the first mode is also well captured in both amplitude and frequency. The dotted curve named as rigid coupling is the FRF obtained by rigidly coupling the blade and the disk models, with a fully rigid connection between them. It can be observed that FRF with rigid coupling is completely different from the Reference one even for the first mode. This validation process, therefore, leads to two main conclusions:

(1) Inserting a joint, after identifying it, between the blade and the disk models is better than rigidly coupling them, since the obtained FRFs are more similar to the measured FRFs of the assembled system.
(2) The set of chosen measurements are suitable to identify the joint in the frequency range around the first mode, while they do not lead to an accurate reconstruction of the FRFs of the jointed system, both in amplitude and in frequency, for a wider frequency range.

4.4 The Joint. The identified joint is a 24×24 DoF system, as mentioned in Sec. 3. Figure 12 shows the plots of dynamic stiffness of one of the translational and rotational DoF versus the frequency. As expected, there are spurious effects which are typical of the identification process [31]. Their presence indicates that some measurement or expansion errors have propagated in the identified joint.

If the only contribution of the joint was the spring stiffness, then the dynamic stiffness of Fig. 12 would be a frequency independent line—known as a zeroth order line. The identified joint dynamic stiffness does not have a straight horizontal line (constant spring stiffness); however, it can be easily seen that a curve can be fit on it. This applies to the dynamic stiffness of both the translational and of the rotational DoF.

The damping effects should be visible at higher frequencies. If the interface exhibits a viscous damping, a frequency-dependent contribution is expected which becomes dominant at higher frequencies. In the case of structural damping, this relation is not as straightforward. Regardless of the type of damping in the joint, its effects should be derivable from the imaginary part of the complex FRF. Unfortunately, due to the limited damping contributions these effects are under the noise floor of the identification procedure, which makes fitting the damping parameters inappropriate.

5 Discussion

In Secs. 3 and 4, a real three-dimensional and a complex structural system of a blade and disk has been tested and expanded with SEMM in order to identify the joint. This has been achieved in following steps:

- validating SEMM on blade and disk as stand-alone substructures through their hybrid models
- identifying a dummy joint's dynamic stiffness with the substructure hybrid models.
- identifying the actual joint
- self-validation of the recoupled system FRF with the actual joint
- on-board validation of the recoupled system FRF with the actual joint (a more restrictive test for the identification)

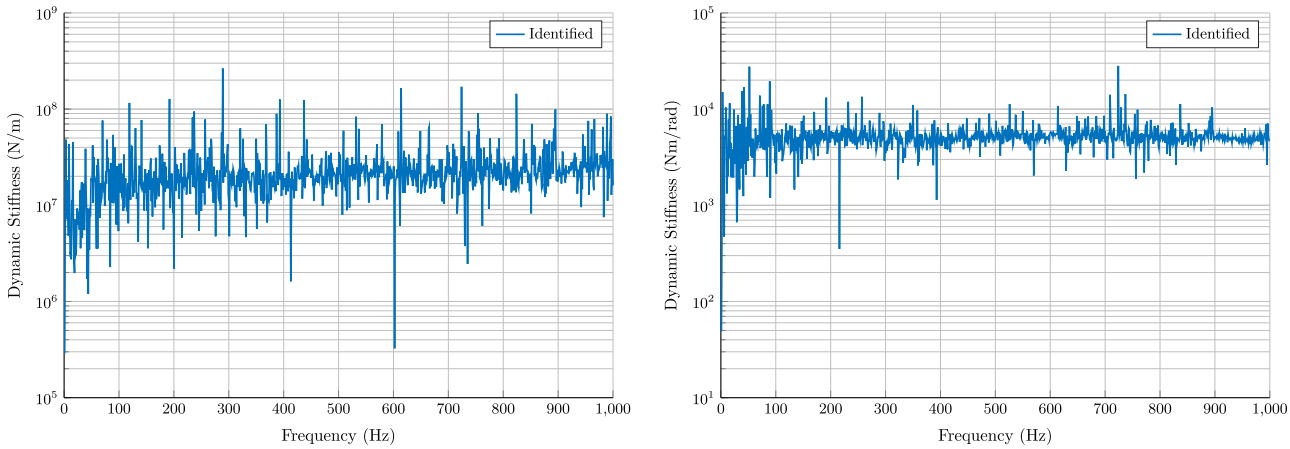

Fig. 12 The identified dynamic stiffness of the actual joint for: (*a*) translational DoF and (*b*) rotational DoF

At each step, some discrepancies have been observed and discussed in the respective sections. As a general observation, the results are affected by various factors including the constraint modeling, choice of internal (measurements) and interface (identification) DoF, and the measurement errors. In this regard, the following aspects should be considered in the future to reduce these effects and improve the joint identification:

(1) The disk should be represented with a different constraint or left unconstrained to reduce the expansion error. As a result, the coupled system should also be tested with the same constraint.
(2) In this work, the interface dynamics were expanded by means of measurement on the internal DoF. It is assumed that the chosen set of DoF could fully observe the interface dynamics. However, this may not be entirely true. A different set of internal DoF could better observe the interface and would thus require a different measurement setup.
(3) Another important aspect in the strategy is the choice of actual interface DoF. A preliminary work on this test-case [18] showed that using two virtual points in the interface was appropriate for the numerical model in the frequency range considered. However, a sensitivity analysis of the type of interface (one, two, or more virtual points or no virtual point) should be performed on the full scale measurement.
(4) The overestimation of the FRF in Fig. 11 can also be due to measurement noise and bias errors and thus should be further investigated.

6 Conclusions

This paper demonstrates that—without the existence of noise—joint identification is possible even when no measurements on the interface are performed. This is achieved by observing dynamics on the internal DoF of stand-alone substructures and expanding to the interface DoF as proposed in SEMM denoted here substructure hybrid models. Extending the SEMM to coupled structures and assuming that the joint dynamics are observed by the internal DoF, the SEMM decoupling method can then be used to identify the joint.

The method is tested on a real three-dimensional academic geometry of a blade and disk having a dove-tail joint. The decoupling method is applied to the experimental measurements of the assembled system to identify the actual joint. The method's identifiability is tested by coupling the identified joint with the hybrid models of the blade and disk. To discern the effect of the joint, two step validation is performed: *self-validation* and *on-board validation*. The former case in which all the FRFs are used in the identification, although a trivial comparison, shows that the joint identification is influenced by measurement and expansion errors.

In the on-board validation, a set of input and output channel is not included in the expansion (a more restrictive check) and compared with re-coupled model (reconstructed FRF by the SEMM decoupling method). The resulting reconstructed FRF captures the first mode's estimation fairly well. However, it altogether overestimates and fails to capture the FRF amplitude for other modes in a wider frequency band. The failure can be attributed to the inability to sufficiently observe and control the true joint, either due to a wrong assumption on the joint geometry (by means of choice of interface DoF) or due to excessive noise and bias errors in the measurements. Unfortunately, these are problems inherent to all FRF-based multi-DoF joint identification techniques and are not restricted to the SEMM-based methodology. The sensitivity of this method to the mentioned problems with respect to comparable methods is not easily quantified and remains to be tested.

In our future research, we aim at improving the joint decoupling by addressing some of the issues regarding measurement and expansion errors discussed in the preceding section. The method will then be extended to identify all the joints of the bladed-disk—being different from each other—leading to experimental understanding of joint mistuning effects in bladed-disks.

Acknowledgment

This work is a part of the project EXPERTISE that received funding from the European Union's H2020 research and innovation program under the Marie Skłodowska-Curie grant agreement No 721865. The authors thank Müller-BBM for lending their hardware PAK-II to perform the measurements and data acquisition. They also acknowledge the support of Vibes Technology for providing Dirac software and Vibes Toolbox for experiment design and post-processing of the data.

Conflict of Interest

There are no conflicts of interest.

Appendix: Convergence of the Iterative Method With Weighted Pseudo Inverses

We recall from Sec. 2.6 that the assembled system's hybrid model was computed by the weighted pseudo inverses in Eqs. (21) and (22). This helps in a faster convergence of the joint properties by assigning higher weights to the physical boundary DoF $\mathbf{u}_b$ and expanding the measured dynamics in a weighted least squares sense.

Figure 13 shows Euclidean norm of the expansion error at each iteration step n for different weights w_b assigned to the physical boundary DoF $\mathbf{u}_b$. The weights of the remaining DoF set are, by default, set to 1. When no weighting value is used for $\mathbf{u}_b$, the convergence is not ensured even after 1000 iterations. This means that the measured dynamics are being expanded equally in all DoF. Thus, the joint or boundary DoF updating and the identification takes more iterations. If SEMM is forced to expand or observe only the boundary DoF, a higher weight is assigned to them. Evidently, the method converges faster when a high weighting value is used for $\mathbf{u}_b$ in Fig. 13. To test the method's convergence, the weights as high as $w_b = 1 \times 10^{14}$ are used. It took only three iterations to convergence at this weight. This implies that SEMM has ignored the internal DoF almost entirely and focused the expansion to the boundary and thus it converged to a hybrid model with minimum expansion error. Such high weightings, though guarantee the method's convergence, were avoided in the joint identification presented in Sec. 4 due to possible numerical issues.

The choice of weights was $w_b = 1 \times 10^8$ for the presented results, unless otherwise stated, due to the fact that the order of stiffness from Fig. 12 is between 10^7 and 10^8.

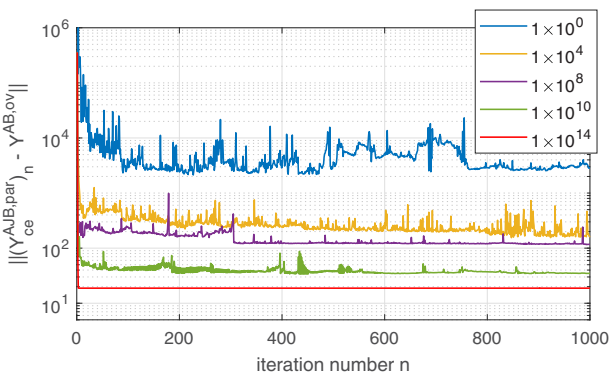

Fig. 13 Effect of weights on the convergence of Euclidean norm of the expansion error between the coupled parent model and the measured overlay model. The physical boundary DoF $\mathbf{u}_b$ is weighted while computing the pseudo inverses, as per Eqs. (21) and (22).

References

[1] De Klerk, D., Rixen, D. J., and Voormeeren, S. N., 2008, "General Framework for Dynamic Substructuring: History, Review, and Classification of Techniques," AIAA J., **46**(5), pp. 1169–1181.

[2] Voormeeren, S. N., and Rixen, D. J., 2012, "A Family of Substructure Decoupling Techniques Based on a Dual Assembly Approach," Mech. Syst. Signal Process., **27**(1), pp. 379–396.

[3] D'Ambrogio, W., and Fregolent, A., 2011, "Direct Decoupling of Substructures Using Primal and Dual Formulation," *Linking Models and Experiments*, Vol. 2, T. Proulx, ed., Springer, New York, NY, pp. 47–76.

[4] Tsai, J. S., and Chou, Y. F., 1988, "The Identification of Dynamic Characteristics of a Single Bolt Joint," J. Sound. Vib., **125**(3), pp. 487–502.

[5] Ren, Y., and Beards, C. F., 1998, "Identification of Effective' Linear Joints Using Coupling and Joint Identification Techniques," J. Vib. Acoust., Trans. ASME, **120**(2), pp. 331–338.

[6] O'Callahan, J.C., Avitable, P., and Riemer, R., 1989, "System Equivalent Reduction Expansion Process," 7th International Modal Analysis Conference, Las Vegas, NV, February.

[7] Thibault, L., Butland, A., and Avitabile, P., 2012, "Variability Improvement of Key Inaccurate Node Groups – VIKING," *Topics in Modal Analysis II*, Vol. 6, R. Allemang, J. De Clerck, C. Niezrecki, and J. R. Blough, eds., Springer, New York, pp. 603–624.

[8] Nicgorski, D., and Avitabile, P., 2010, "Conditioning of FRF Measurements for Use with Frequency Based Substructuring," Mech. Syst. Signal Process., **24**(2), pp. 340–351.

[9] Allen, M. S., Mayes, R. L., and Bergman, E. J., 2010, "Experimental Modal Substructuring to Couple and Uncouple Substructures With Flexible Fixtures and Multi-point Connections," J. Sound. Vib., **329**(23), pp. 4891–4906.

[10] Laxalde, D., Lombard, J. P., and Thouverez, F., 2007, "Dynamics of Multistage Bladed Disks Systems," ASME J. Eng. Gas. Turbines. Power., **129**(4), pp. 1058–1064.

[11] Klaassen, S. W., van der Seijs, M. V., and de Klerk, D., 2018, "System Equivalent Model Mixing," Mech. Syst. Signal Process., **105**(Dec.), pp. 90–112.

[12] Rixen, D. J., 2008, "How Measurement Inaccuracies Induce Spurious Peaks in Frequency Based Substructuring," International Modal Analysis Conference, Orlando, FL, January.

[13] Ewins, D. J., 2000, *Modal Testing: Theory, Practice and Application*, Research Studies Press Ltd., Baldock, Hertfordshire, England.

[14] Harvie, J., and Avitabile, P., 2014, "Effects of Precise FRF Measurements for Frequency Based Substructuring," *Topics in Experimental Dynamic Substructuring*, Vol. 2, R. Mayes, D. Rixen, and M. Allen, eds., Springer, New York, pp. 277–285.

[15] Zhen, J., Lim, T. C., and Lu, G., 2004, Determination of System Vibratory Response Characteristics Applying a Spectral-Based Inverse Sub-structuring Approach. Part I: Analytical Formulation. Technical Report 2.

[16] Ewins, D. J., 1980, "On Predicting Point Mobility Plots From Measurements of Other Mobility Parameters," J. Sound. Vib., **70**(1), pp. 69–75.

[17] Moorhouse, A., and Elliott, A., 2013, "The Round Trip Theory for Reconstruction of Green's Functions At Passive Locations," J. Acoust. Soc. Am., **134**(5), pp. 3605–3612.

[18] Saeed, Z., Firrone, C. M., and Berruti, T. M., 2019, "Substructuring for Contact Parameters Identification in Bladed-disks," J. Phys.: Conf. Ser., **1264**(1), p. 012037.

[19] Saeed, Z., Jenovencio, G., Arul, S., Blahoš, J., Sudhakar, A., Pesaresi, L., Yuan, J., El Haddad, F., Hetzler, H., and Salles, L., 2020, "A Test-Case on Continuation Methods for Bladed-Disk Vibration With Contact and Friction," *Nonlinear Structures and Systems*, Vol. 1, G. Kerschen, M. Brake, and L. Renson, eds., Springer, Cham.

[20] D'Ambrogio, W., and Fregolent, A., 2014, "Are Rotational DoFs Essential in Substructure Decoupling?" *Dynamics of Coupled Structures*, Vol. 1, M. Allen, R. Mayes, and D. Rixen, eds., Springer, Cham, pp. 27–36.

[21] Drozg, A., Čepon, G., and Boltežar, M., 2018, "Full-Degrees-of-Freedom Frequency Based Substructuring," Mech. Syst. Signal Process., **98**, pp. 570–579.

[22] Čepon, G., Drozg, A., and Boltežar, M., 2019, "Introduction of Line Contact in Frequency-based Substructuring Process Using Measured Rotational Degrees of Freedom," J. Phys. Conference Series, **1264**, pp. 344–355.

[23] Bregar, T., Holeček, N., Čepon, G., Rixen, D. J., and Boltežar, M., 2019, "Including Directly Measured Rotations in the Virtual Point Transformation," Mech. Syst. Signal Process., **141**, p. 106440.

[24] Duarte, M. L. M., and Ewins, D. J., 2000, "Rotational Degrees of Freedom for Structural Coupling Analysis Via Finite-difference Technique with Residual Compensation," Mech. Syst. Signal Process., **14**(2), pp. 205–227.

[25] De Klerk, D., Rixen, D. J., Voormeeren, S. N., and Pasteuning, F., 2008, Solving the RDoF Problem in Experimental Dynamic Substructuring, Technical Report.

[26] Van Der Seijs, M. V., Van Den Bosch, D. D., Rixen, D. J., and De Klerk, D., 2013, "An Improved Methodology for the Virtual Point Transformation of Measured Frequency Response Functions in Dynamic Substructuring," COMPDYN, Greece, June.

[27] Meggitt, J. W., Elliott, A. S., Moorhouse, A. T., and Lai, H. K., 2015, "In Situ Determination of Dynamic Stiffness for Resilient Elements," Proc. Inst. Mech. Eng., Part C: J. Mech. Eng. Sci., **230**(6), pp. 986–993.

[28] Keersmaekers, L., Mertens, L., Penne, R., Guillaume, P., and Steenackers, G., 2015, "Decoupling of Mechanical Systems Based on In-situ Frequency Response Functions: The Link-Preserving, Decoupling Method," Mech. Syst. Signal Process., **58–59**, pp. 340–354.

[29] Haeussler, M., Klaassen, S. W. B., and Rixen, D. J., 2018, "Comparison of Substructuring Techniques for Experimental Identification of Rubber Isolators Dynamic Properties," ISMA 2018—International Conference on Noise and Vibration Engineering, Leuven, Belgium, Sept. 17–19.

[30] Batista, F. C., and Maia, N. M., 2012, "An Iterative Uncoupling Technique for the Identification of the Dynamic Properties of Joints," ISMA 2012 – International Conference on Noise and Vibration Engineering, Leuven, Belgium, Sept. 17–19.

[31] Tol, C., and Özgüven, H. N., 2015, "Dynamic Characterization of Bolted Joints Using FRF Decoupling and Optimization," Mech. Syst. Signal Process., **54–55**, pp. 124–138.

[32] Haeussler, M., Klaassen, S. W., and Rixen, D. J., 2020, "Experimental Twelve Degree of Freedom Rubber Isolator Models for Use in Substructuring Assemblies," J. Sound. Vib., **474**, pp. 115253.

[33] Klaassen, S. W., and Rixen, D. J., 2020, "Using SEMM to Identify the Joint Dynamics in Multiple Degrees of Freedom Without Measuring Interfaces," *Dynamic Substructures*, Vol. 4, A. Linderholt, M. Allen, and R. Mayes, eds., Springer, Cham, pp. 87–99.

[34] De Klerk, D., Rixen, D. J., and De Jong, J., 2006, "The Frequency Based Substructuring (FBS) Method Reformulated According to the Dual Domain Decomposition Method," Fifteenth International Modal Analysis Conference, St. Louis, MO, February.

[35] Sjövall, P., and Abrahamsson, T., 2008, "Substructure System Identification From Coupled System Test Data," Mech. Syst. Signal Process., **22**(1), pp. 15–33.

[36] Craig, R. R., and Bampton, M. C. C., 1968, "Coupling of Substructures for Dynamic Analyses," AIAA J., **6**(7), pp. 1313–1319.

[37] Smith, S., Bilbao-Ludena, J. C., Catalfamo, S., Brake, M. R., Reuß, P., and Schwingshackl, C. W., 2016, "The Effects of Boundary Conditions, Measurement Techniques, and Excitation Type on Measurements of the Properties of Mechanical Joints," *Nonlinear Dynamics*, Vol. 1, G. Kerschen, ed., Springer, Cham.